

UC Berkeley

UC Berkeley Previously Published Works

Title

Exploring the $\text{Pb}_{1-x}\text{Sr}_x\text{HfO}_3$ System and Potential for High Capacitive Energy Storage Density and Efficiency

Permalink

<https://escholarship.org/uc/item/35z1n5xh>

Journal

Advanced Materials, 34(1)

ISSN

0935-9648

Authors

Acharya, Megha
Banyas, Ella
Ramesh, Maya
[et al.](#)

Publication Date

2022

DOI

10.1002/adma.202105967

Peer reviewed

Exploring the $\text{Pb}_{1-x}\text{Sr}_x\text{HfO}_3$ System and Potential for High Capacitive Energy Storage Density and Efficiency

Megha Acharya, Ella Banyas, Maya Ramesh, Yizhe Jiang, Abel Fernandez, Arvind Dasgupta, Handong Ling, Brendan Hanrahan, Kristin Persson, Jeffrey B. Neaton, and Lane W. Martin*

The hafnate perovskites PbHfO_3 (antiferroelectric) and SrHfO_3 (“potential” ferroelectric) are studied as epitaxial thin films on SrTiO_3 (001) substrates with the added opportunity of observing a morphotropic phase boundary (MPB) in the $\text{Pb}_{1-x}\text{Sr}_x\text{HfO}_3$ system. The resulting (240)-oriented PbHfO_3 (*Pba2*) films exhibited antiferroelectric switching with a saturation polarization $\approx 53 \mu\text{C cm}^{-2}$ at 1.6 MV cm^{-1} , weak-field dielectric constant ≈ 186 at 298 K, and an antiferroelectric-to-paraelectric phase transition at $\approx 518 \text{ K}$. (002)-oriented SrHfO_3 films exhibited neither ferroelectric behavior nor evidence of a polar *P4mm* phase. Instead, the SrHfO_3 films exhibited a weak-field dielectric constant ≈ 25 at 298 K and no signs of a structural transition to a polar phase as a function of temperature (77–623 K) and electric field (-3 to 3 MV cm^{-1}). While the lack of ferroelectric order in SrHfO_3 removes the potential for MPB, structural and property evolution of the $\text{Pb}_{1-x}\text{Sr}_x\text{HfO}_3$ ($0 \leq x < 1$) system is explored. Strontium alloying increased the electric-breakdown strength (E_B) and decreased hysteresis loss, thus enhancing the capacitive energy storage density (U_c) and efficiency (η). The composition, $\text{Pb}_{0.5}\text{Sr}_{0.5}\text{HfO}_3$ produced the best combination of $E_B = 5.12 \pm 0.5 \text{ MV cm}^{-1}$, $U_c = 77 \pm 5 \text{ J cm}^{-3}$, and $\eta = 97 \pm 2\%$, well out-performing PbHfO_3 and other antiferroelectric oxides.

have been found to be promising for capacitive energy storage applications as compared to their ferroelectric and dielectric counterparts.^[9–11] Among the range of materials that could be studied, two potentially exciting hafnate perovskite oxides are PbHfO_3 and SrHfO_3 . PbHfO_3 (*Pba2*, lattice parameters: $a = 5.854 \text{ \AA}$, $b = 11.694 \text{ \AA}$, $c = 8.191 \text{ \AA}$ ^[12]) has been synthesized and its structural,^[13,14] optical,^[15] and dielectric^[16] properties have been probed in bulk ceramics and single crystals. It exhibits a switching-field-induced phase transition from an antiferroelectric *Pbam* to a ferroelectric *Pba2* phase at $\approx 250 \text{ kV cm}^{-1}$, characterized by a double polarization-hysteresis loop. PbHfO_3 is isostructural to the archetypal antiferroelectric PbZrO_3 (*Pba2*, lattice parameters: $a = 5.88 \text{ \AA}$, $b = 11.77 \text{ \AA}$, $c = 8.22 \text{ \AA}$ ^[17]), has a large bandgap (3.4 eV ^[18]), and a dielectric constant ≈ 90 at room temperature.^[12] There have been a few reports wherein PbHfO_3 has been produced as polycrystalline thin films

1. Introduction

Hafnate-based thin films, in both perovskite^[1,2] and non-perovskite^[3,4] phases, have garnered extensive attention owing to their potential application as gate materials and/or ferroelectric memories in complementary metal-oxide-semiconductor (CMOS) devices. Additionally, many antiferroelectric hafnate systems^[5–8]

including those produced by atomic-layer deposition^[19–21] and the antiferroelectric, electrocaloric, and energy-storage properties have been explored.

SrHfO_3 has also been synthesized using solid-state reaction methods and its structural properties examined.^[22] In the bulk, SrHfO_3 exhibits a *Pnma* structure at ambient conditions. Other polymorphs (i.e., *Cmcm*, *I4/mcm*, *Pmm*) are observed


M. Acharya, M. Ramesh, Y. Jiang, A. Fernandez, A. Dasgupta, H. Ling, K. Persson, L. W. Martin
Department of Materials Science and Engineering
University of California, Berkeley
Berkeley, CA 94720, USA
E-mail: lwmartin@berkeley.edu

M. Acharya, E. Banyas, K. Persson, J. B. Neaton, L. W. Martin
Materials Sciences Division
Lawrence Berkeley National Laboratory
Berkeley, CA 94720, USA
B. Hanrahan
U.S. Army Research Laboratory
Adelphi, MD 20783, USA

K. Persson, J. B. Neaton
Molecular Foundry
Lawrence Berkeley National Laboratory
Berkeley, CA 94720, USA

J. B. Neaton
Department of Physics
University of California, Berkeley
Berkeley, CA 94720, USA

J. B. Neaton
Kavli Energy Nanosciences Institute
University of California
Berkeley, CA 94720, USA

 The ORCID identification number(s) for the author(s) of this article can be found under <https://doi.org/10.1002/adma.202105967>.

DOI: 10.1002/adma.202105967

upon heating-induced structural-phase transitions by virtue of changes in the HfO_6 octahedral-tilt angles. Studies of the dielectric^[23] and optical^[24] properties revealed low dielectric constant (17–25^[25]) and large bandgap (6.1 eV^[22]). While there has been speculation about the appearance of temperature-induced soft-phonon modes in the $Cmcm$ and $I4/mcm$ phases, these were found to be associated with octahedral rotations. Similarly, the dominant lattice instabilities in the $Pm\bar{3}m$ phase have also been shown in experimental and theoretical studies to be associated with antiferrodistortive modes, leading to nonpolar phases that do not give rise to ferroelectric behavior.^[23,26] This said, a recent report focused on epitaxial thin films^[27] suggested a tetragonal $P4mm$ structure can be produced which gives rise to a piezoelectric response ($\epsilon_{33} = 8.8 \text{ C m}^{-2}$) and further suggests that this phase could be ferroelectric. Despite these interesting observations there is little work, especially on thin films of both systems, and the true nature of properties of these potentially interesting materials as thin films could stand to be better understood.

While additional studies of thin films of the parent compounds are warranted, an intriguing possibility is also presented as it relates to solid solutions of these materials (i.e., $\text{Pb}_{1-x}\text{Sr}_x\text{HfO}_3$). First, the combination of the antiferroelectric $Pbam$ PbHfO_3 and (potentially) ferroelectric $P4mm$ SrHfO_3 ^[27] could give rise to a morphotropic phase boundary (MPB), analogous to that in the well-studied $\text{PbZr}_x\text{Ti}_{1-x}\text{O}_3$ (PZT) system. Recent ab initio predictions have shown that even apart from a prospective structural-phase boundary, $\text{Pb}_{1-x}\text{Sr}_x\text{HfO}_3$ could exhibit enhanced piezoresponse as a function of ionic disorder (associated with the strontium alloying).^[28] Finally, strontium alloying is well known to improve the leakage and breakdown strength of lead-based perovskites^[29] and thus there is potential that the $\text{Pb}_{1-x}\text{Sr}_x\text{HfO}_3$ system could provide a pathway to improved capacitive energy storage performance. The key parameters underlying capacitive-energy storage of any dielectric material are the recoverable energy density in the charge–discharge process ($U_r = \int_{P_{\text{max}}}^P E dP$, where P_r and P_{max} are the remanent and maximum polarization, respectively) and the energy-storage loss (U_{loss} , which is determined by the area enclosed within the double hysteresis loops). U_r and U_{loss} dictate the overall efficiency in the charge–discharge process [$\eta = (U_r / (U_r + U_{\text{loss}}))$].^[30] Multiple design strategies have been adopted to enhance the U_r and η values in antiferroelectric materials with chemical alloying^[31–33] being a common choice and it is possible that in $\text{Pb}_{1-x}\text{Sr}_x\text{HfO}_3$ such an approach could be effective due to reduced leakage, improved breakdown strength, and increased polarization in the parent antiferroelectric PbHfO_3 .

Here, we synthesize epitaxial $\text{Pb}_{1-x}\text{Sr}_x\text{HfO}_3$ ($x = 0, 0.05, 0.15, 0.25, 0.5, 0.75, 1$) thin films across a range of temperatures, oxygen partial pressures, substrates, laser fluences, etc., to explore this system. The results are organized into three sections. The first, focuses on PbHfO_3 thin films wherein (240_{O})-oriented ($Pbam$; the subscript “O” represents lattice indexing for the orthorhombic structure) films which exhibit robust antiferroelectric behavior and undergo an electric-field-induced phase transition to a ferroelectric phase ($Pba2$). The measured polarization was $53 \mu\text{C cm}^{-2}$ at 1.6 MV cm^{-1} with a weak-field dielectric constant ≈ 186 at 298 K and a dielectric

anomaly centered at $\approx 518 \text{ K}$, characteristic of the antiferroelectric-to-paraelectric phase transition. The second section focuses on SrHfO_3 thin films wherein (002)-oriented ($Pm\bar{3}m$) films were produced. Despite extensive study, no evidence of polar order was observed as a function of temperature and/or applied electric field. The measured polarization was $0.3 \mu\text{C cm}^{-2}$ at 3 MV cm^{-1} with a weak-field dielectric constant ≈ 25 at 298 K. Finally, the last section focuses on 75-nm-thick (240_{O})-oriented $\text{Pb}_{1-x}\text{Sr}_x\text{HfO}_3$ ($0 < x < 1$) films. While the absence of polar, ferroelectric behavior in the SrHfO_3 films meant that MPB phenomena akin to those in the PZT system is improbable, strong impact on the evolution of the polarization-electric field response (and therefore capacitive energy storage properties) were found. Increasing strontium content enhances the electric-breakdown strength (E_B) and decreases U_{loss} , both of which play a critical role in increasing the U_r and η values. $\text{Pb}_{0.5}\text{Sr}_{0.5}\text{HfO}_3$ was found to exhibit the highest E_B (5.12 MV cm^{-1} ; three times the value of 1.23 MV cm^{-1} for PbHfO_3), a 6% increase in the η values (from 91% for PbHfO_3 to 97%), a 2.7 times increase in U_r (from 21 J cm^{-3} for PbHfO_3 to 77 J cm^{-3}), and a 10^6 times improvement in fatigue endurance at $E_B = 1.23 \text{ MV cm}^{-1}$. This performance places $\text{Pb}_{0.5}\text{Sr}_{0.5}\text{HfO}_3$ among the most promising antiferroelectrics for such applications.

2. Results and Discussion

2.1. PbHfO_3

Motivated by the multiple studies probing the energy-storage properties of antiferroelectric oxides due to their unique property of undergoing an antiferroelectric-to-ferroelectric phase transition upon application of electric field,^[29,33,34] we synthesized and characterized single-crystalline antiferroelectric PbHfO_3 films. In the current work, $15\text{--}360\text{-nm-thick}$ (240_{O})-oriented PbHfO_3 (Figure 1a) films were deposited on a range of substrates at a range of growth conditions using pulsed-laser deposition (Experimental Section). For brevity, X-ray diffraction scans have been included for 75-nm-thick films grown at a fixed heater temperature ($650 \text{ }^\circ\text{C}$), laser fluence (1.7 J cm^{-2}), and variable dynamic oxygen-partial pressure ($10\text{--}100 \text{ mTorr}$) using $45\text{--}55\text{-nm-thick}$ SrRuO_3 layers as the top and bottom electrodes (Figure 1b). Rutherford backscattering spectrometry (Experimental Section) was used to probe the film stoichiometry. The growth pressure can be used to control the Pb:Hf ratio in the PbHfO_3 heterostructures (Figure S1, Supporting Information) whereby decreasing the oxygen-partial pressure during growth from 100 to 10 mTorr (at a fixed laser fluence and heater temperature of 1.1 J cm^{-2} and $600 \text{ }^\circ\text{C}$, respectively) resulted in a decrease in the Pb:Hf ratio (i.e., decrease in the percentage of the heavier cation, Pb^{2+}) in the films with optimized chemistry found for growth at $\approx 30 \text{ mTorr}$. Such trends are similar to those observed in other perovskite oxides.^[35]

The epitaxy of the PbHfO_3 films was determined using off-axis azimuthal (ϕ) scans (Experimental Section). Scans were completed about the SrTiO_3 (substrate) 103- and PbHfO_3 (film) 362_{O} -diffraction conditions, wherein the substrate is expected and observed to have four peaks (Figure 1c) and the $Pbam$ phase of PbHfO_3 is expected to exhibit two peaks (i.e., 362_{O} and

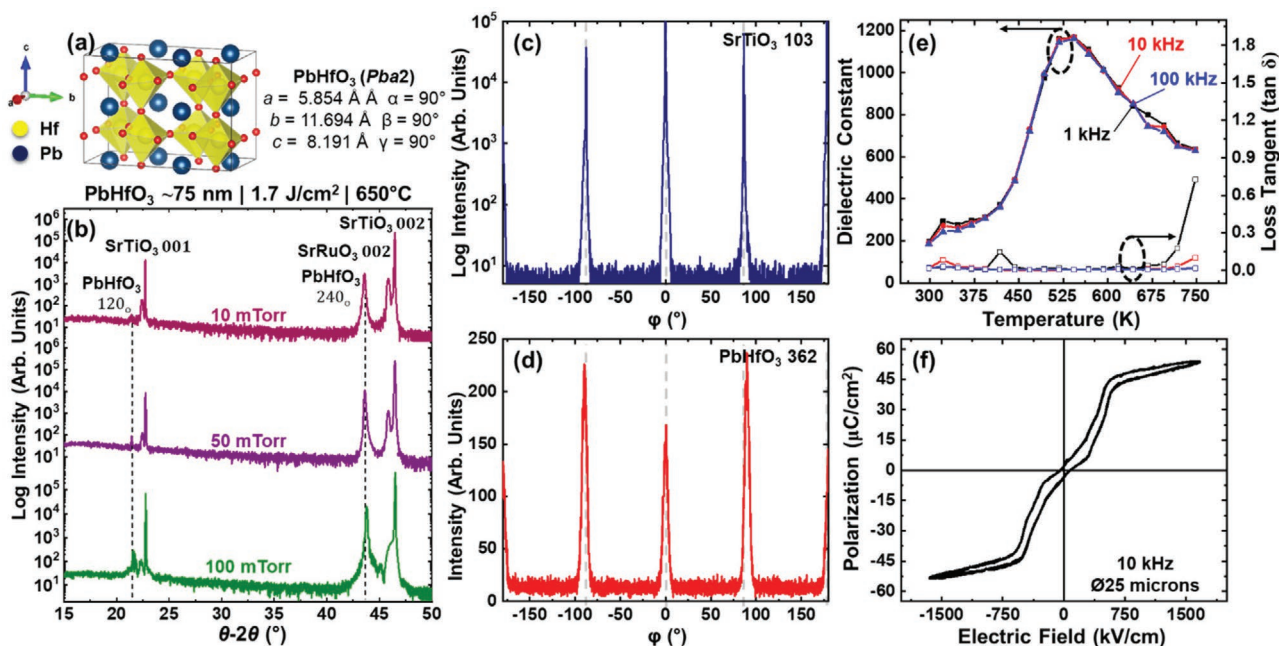


Figure 1. Structural, dielectric, and antiferroelectric properties of epitaxial PbHfO₃ thin films. a) Crystal structure and lattice parameters for orthorhombic antiferroelectric phase of PbHfO₃ (*Pba2*). b) X-ray-diffraction measurement (wide-angle θ - 2θ line scan) for 75-nm-thick (240_O)-oriented PbHfO₃ films on SrTiO₃ (001) substrates as a function of dynamic oxygen-partial pressure during growth (top to bottom, growth at 10, 50, and 100 mTorr) with a fixed heater temperature (650 °C) and laser fluence (1.7 J cm⁻²). Azimuthal φ scans about the c) SrTiO₃ 103-diffraction condition and the d) PbHfO₃ 362_O-diffraction condition. e) Temperature-dependent dielectric constant (left axis) and loss tangent (right axis) measurements from 298 to 750 K at 1, 10, and 100 kHz. f) Polarization versus electric field hysteresis loops at room temperature at a frequency of 10 kHz for capacitors 25 μ m in diameter.

362_O) separated by $\varphi = 180^\circ$. The azimuthal scan (Figure 1d), however, revealed the presence of four peaks for the PbHfO₃ which is consistent with the presence of two rotational structural variants (labeled I and II; Figure S2, Supporting Information), rotated by 90° with respect to each other (such that they align with the peaks for the SrTiO₃ substrate). Thus, the epitaxy is found to be PbHfO₃ [001_O] || SrTiO₃ [010] for rotational variant I and PbHfO₃ [001_O] || SrTiO₃ [100] for rotational variant II with PbHfO₃ [240_O] || SrTiO₃ [001] for both cases. The lattice parameters were determined to be $a_o = 5.88 \pm 0.005$ Å, $b_o = 11.63 \pm 0.005$ Å, and $c_o = 8.30 \pm 0.005$ Å (consistent with an orthorhombic crystal structure) using reciprocal space mapping (RSM) studies about the 084_O- and 362_O-diffraction conditions of the PbHfO₃ (Figure S3, Supporting Information).

Having determined the crystal structure and chemical composition of the epitaxial films, the electrical properties of the PbHfO₃ heterostructures were also probed. In the bulk, PbHfO₃ has been reported to undergo two structural phase transitions. The first is to another antiferroelectric phase (the crystal structure and space-group symmetry of which has not yet been established) at 436 K which is unlikely to be resolved in dielectric measurements for thin films.^[20] The second is a transition to the paraelectric cubic phase (*Pm* $\bar{3}$ *m*) reported to be in the temperature range of 476–484 K.^[16,36,37,38] The dielectric constant and loss as a function of temperature for the films produced herein display evidence of a phase transition from the antiferroelectric (*Pba2*) to the paraelectric (*Pm* $\bar{3}$ *m*) phase at ≈ 518 K (Figure 1e).^[37,38] All the synthesized heterostructures exhibited a double-hysteresis loop in their polarization response indica-

tive of antiferroelectric behavior.^[39] The relatively high leakage current density in the PbHfO₃ films grown at high pressures (100 mTorr), however, was found to prevent the measurement of fully saturated double-hysteresis loops (Figure S4, Supporting Information). Apart from modifying the Pb:Hf ratio in the synthesized thin films, changes in the growth pressure played a critical role in our ability to observe the antiferroelectric properties of the PbHfO₃ heterostructures. Decreasing the growth pressure is expected to introduce a multitude of structural point defects as well as defect clusters owing to the knock-on damage induced by the enhanced kinetic energy of the incident adatoms. The presence of such defects in ferroelectric PbTiO₃ has been shown to produce deep-trap states (which cannot be readily activated) associated with defect complexes resulting in enhanced resistivity.^[40,41] The defect clusters can be composed of cation and/or anion vacancies and potential interstitials or antisites.^[42] Using the same hypothesis, we observed an increase in the maximum electric field that can be applied to the PbHfO₃ heterostructures from 1 MV cm⁻¹ (100 mTorr) to 1.23 MV cm⁻¹ (10 mTorr; Figure 1f and Figure S4, Supporting Information) with substantial reduction in the leakage current density. The ability to obtain fully saturated and slim double-hysteresis loops in the polarization response helped in determining the true energy-storage parameters of the PbHfO₃ films. Additionally, the substitution of lead with strontium is expected to affect the polar ordering and enhance the stability of the antiferroelectric state.^[29] There are no reports, however, demonstrating the same for PbHfO₃ heterostructures, making a systematic study of strontium alloying, especially worthwhile.

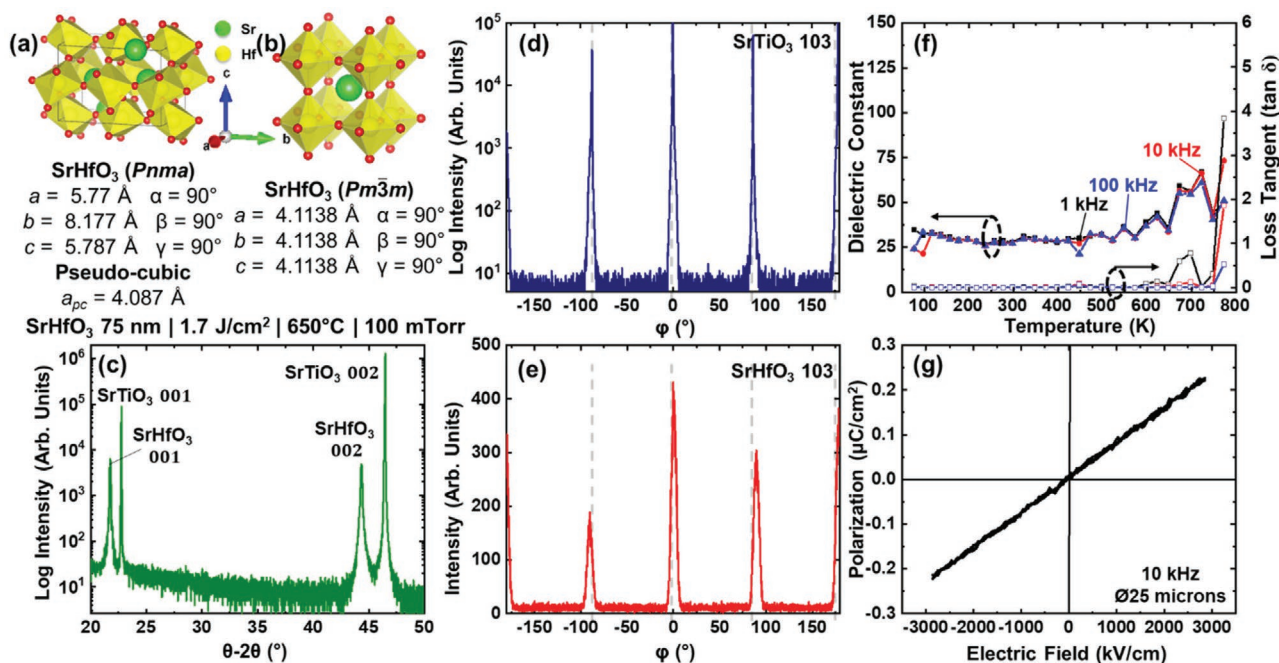


Figure 2. Structural, dielectric, and polarization response of epitaxial SrHfO₃ thin films. Crystal structure and lattice parameters for a) orthorhombic (*Pnma*) and b) cubic (*Pm3m*) phases. c) X-ray diffraction measurement (wide-angle θ - 2θ line scan) for 75-nm-thick (001)-oriented SrHfO₃ on a SrTiO₃ (001) substrate grown at a heater temperature (650 °C), laser fluence (1.7 J cm⁻²), and at dynamic oxygen partial pressure 100 mTorr during growth. Azimuthal scans about the d) SrTiO₃ 103-diffraction condition and e) SrHfO₃103-diffraction condition. f) Temperature-dependent dielectric constant (left axis) and loss tangent (right axis) measurements from 77 to 750 K at 1, 10, and 100 kHz. g) Polarization versus electric field hysteresis loops at room temperature at a frequency of 10 kHz for capacitors 25 μ m in diameter.

2.2. SrHfO₃

SrHfO₃ has been synthesized and studied in various polymorphic forms (Figure 2a,b and Figure S5, Supporting Information). The presence of a metastable polar, piezoelectric SrHfO₃ (*P4mm*) phase has recently been reported.^[27] To investigate the structure and properties of SrHfO₃ thin films, we synthesized highly crystalline (001)_{pc}-oriented SrHfO₃ (subscript “pc” represents pseudocubic) on SrTiO₃ (001) ($a = 3.905$ Å) and other substrates (Experimental Section) as confirmed by X-ray diffraction measurements (Figure 2c). Further, RSM studies (Figure S6, Supporting Information) performed about the SrHfO₃ 103_{pc}- and 101_{pc}-diffraction conditions were used to extract the lattice parameters as $a_{pc} = 4.08 \pm 0.005$ Å, $b_{pc} = 4.07 \pm 0.005$ Å, and $c_{pc} = 4.08 \pm 0.005$ Å. The extracted $c/a = 1.0004$ (≈ 1) accompanied with the reports about synthesis of a cubic crystal symmetry of SrHfO₃ as thin films in the literature^[2,24,48,49] suggests that the crystal structure of the as-grown SrHfO₃ phase is likely to be a cubic (*Pm3m*) symmetry as well. High-quality crystalline SrHfO₃ thin films (with cubic *Pm3m* symmetry) were obtained on NdScO₃ (110) substrates as well. We do note the formation of a minority secondary phase—likely the thermodynamically stable SrHfO₃ (*Pnma*) phase—for some combinations of total laser pulses (or the film thickness), partial pressure of oxygen, and temperature (Figure S7, Supporting Information). Off-axis azimuthal (φ) scans about the 103-diffraction condition for both the substrate (Figure 2d) and film (Figure 2e) revealed the epitaxy to be SrHfO₃ [100] || SrTiO₃ [100], SrHfO₃ [010] || SrTiO₃ [010], and SrHfO₃ [001] || SrTiO₃ [001].

We proceeded to perform electrical characterization to search for evidence of a structural-phase transition (commensurate with a dielectric anomaly) to the *P4mm* phase. The dielectric constant and loss (Figure 2f and Figure S8, Supporting Information) were measured as a function of temperature (77–623 K) and reveal a weak-field dielectric constant ≈ 25 at room temperature and no evidence of an anomaly across the temperature range probed herein. Such behavior has been seen in CdTiO₃^[43] which undergoes a structural phase transition below room temperature (77 K) from a non-polar (*Pnma*) to a polar (*Pna21*) phase. Polarization-electric field measurements (from –3 to 3 MV cm⁻¹) were completed as a function of temperature (77–623 K) and reveal low polarization response (≈ 0.3 μ C cm⁻² at maximum field) for 33–400-nm-thick SrHfO₃ heterostructures grown on SrRuO₃-buffered SrTiO₃ (001) (Figure 2g). Again, there was an absence of nonlinearity or hysteresis in the polarization response across the entire temperature range studied. Taken together, this suggests that the SrHfO₃ films produced here are not ferroelectric across the temperature range (77–623 K) nor under applied electric field (–3 to 3 MV cm⁻¹).

The observation of the cubic (*Pm3m*) SrHfO₃ phase and the absence of ferroelectric behavior led us to examine this material in more detail, akin to prior studies.^[44] Although, prior first-principles density functional theory (DFT) calculations of the phonon spectra of the bulk SrHfO₃ (*Pm3m*) phase reported the presence of zone-center polar instabilities; the same calculations show that the dominant phonon instabilities are associated with antiferrodistortive zone-boundary modes. This result is consistent with the observed low-temperature, non-polar ground state (i.e., the *Pnma*

phase).^[45,46] While the stabilization of the cubic crystal symmetry in thin films indicates a suppression of the antiferrodistortive modes, the absence of a $P4mm$ phase further suggests that the ferroelectric instability was likewise suppressed. Using DFT within the local density approximation (LDA), we examined the energy landscape across the structural distortion from the nonpolar to the polar phase^[47] (Experimental Section). A small monotonic decrease in energy was computed along a polar distortion path (0.62 meV/atom for DFT-LDA; Figure S9a, Supporting Information). When compared to the DFT-LDA calculations of the energy differences between the $Pm\bar{3}m$ and $P4mm$ structures in the known ferroelectrics^[48] [e.g., $PbTiO_3$ ($\Delta E = 11.6$ meV/atom) and $BaTiO_3$ ($\Delta E = 1.0$ meV/atom)], the smaller energy difference for $SrHfO_3$, combined with the presence of zone-boundary instabilities, are consistent with the lack of appearance of the $P4mm$ phase in the synthesized films. Similar results were obtained for DFT-Perdew-Burke-Ernzerhof (PBE) calculations as well (Figure S9b, Supporting Information). In summary, the DFT calculations performed here along with prior ones in the literature are consistent with the absence of any significant polar distortion or hysteresis in the polarization response of the as-grown $SrHfO_3$ films. Additionally, prior work for bulk $SrHfO_3$ corroborates the fact that we did not find any evidence of a tetragonal ($P4mm$) structure despite extensive electrical studies across a wide temperature range.^[23,22,49] Other experimental studies of $SrHfO_3$ thin films, including those looking at its growth on semiconductor substrates such as Si (001) and Ge (001)^[24,46,50] also report a suppression of all instabilities, similar cubic structures, and relatively low dielectric constant (≈ 30). Additionally, Raman spectroscopy investigating the temperature-induced soft-phonon modes in the $SrHfO_3$ polymorphs suggests the possibility of modes that would give rise to antiferrodistortive character rather than ferrodistortive character.^[23] Consistent with these works, at least for the growth conditions explored here, the stable phase of $SrHfO_3$ in the synthesized thin films is found to be cubic and non-polar.

With the absence of ferroelectric behavior in the $SrHfO_3$ films, the possibility of a structural phase-boundary akin to the MPB in PZT across the $PbHfO_3$ - $SrHfO_3$ solid solution seemed unlikely. We did, however, observe antiferroelectric switching behavior and low dielectric loss in the synthesized $PbHfO_3$ thin films, necessitating further studies in the same and the exploration of the $Pb_{1-x}Sr_xHfO_3$ system as a pathway to further improve performance. There have been similar studies on strontium alloying in $PbZrO_3$ as bulk ceramics. Especially with the slightly smaller ionic radius of Sr^{2+} cations, the tolerance factor of the solid solutions is expected to be lower than $PbZrO_3$, resulting in an increased Curie temperature and a more stable antiferroelectric phase with a lower dielectric constant and hysteresis loss.^[29] Prior studies of the $Pb_{1-x}Sr_xZrO_3$ system also do not explore the entire phase diagram (i.e., beyond $x = 0.05$). Though not useful as a ferroelectric, $SrHfO_3$ is likely to improve the antiferroelectric and energy-storage properties of $PbHfO_3$ when synthesized as a solid solution.

2.3. $PbHfO_3$ - $SrHfO_3$ Solid Solutions

With the desire to alter the properties of $PbHfO_3$, we proceeded to explore the synthesis and energy-storage properties

of $Pb_{1-x}Sr_xHfO_3$ thin films. We synthesized and characterized epitaxial $Pb_{1-x}Sr_xHfO_3$ ($x = 0.05, 0.15, 0.25, 0.5, 0.75$) thin films using similar conditions and approaches (Experimental Section). With the difference between the ionic radii of Pb^{2+} (149 pm) and Sr^{2+} (144 pm) ions being small (3% difference), isovalent substitution is expected to be feasible while forming a stable single-phase solid solution. Following synthesis of the $Pb_{1-x}Sr_xHfO_3$ compounds, X-ray diffraction studies were completed to probe the evolution of the crystal structure. Highly crystalline, single-phase, solid-solution films were obtained for all compositions explored (Figure 3). The crystallinity of the synthesized films with respect to the substrate was ascertained using rocking curves and azimuthal (ϕ) scans (Figures S10 and S11, Supporting Information). The $Pb_{1-x}Sr_xHfO_3$ ($0 < x < 1$) 240_O-diffraction peaks, in all cases, appear to shift (minimally) to higher $\theta-2\theta$ values (i.e., corresponding a reduction of the out-of-plane lattice parameter) with increasing strontium content. This is expected due to the isovalent substitution of a (slightly) smaller-sized Sr^{2+} cation at the Pb^{2+} site. Additional RSM studies were performed about the 362_O- and 084_O-diffraction conditions of $PbHfO_3$ and the 103-diffraction condition of the $SrTiO_3$ (001) substrate (Figure S12a-j, Supporting Information) to obtain the lattice parameters (with an error bar of ± 0.005 Å) of all the compositions. The overall change in all the three lattice parameters (a , b , and c) with respect to that of the parent $PbHfO_3$ was found to be minimal. Again, this can be rationalized from the fact that there is only a small difference (3%) in the ionic radii of the Sr^{2+} and Pb^{2+} cations (Figure S12k-l, Supporting Information).

Although all the $Pb_{1-x}Sr_xHfO_3$ compositions appear isostructural, they exhibited a varied range of electrical properties. Frequency-dependent studies of the dielectric constant (Figure 4a) reveal that increasing strontium content results in a reduction in the dielectric constant from ≈ 186 for $x = 0$ to ≈ 25 for $x = 1$ (the loss remains low for all compositions; Figure S13, Supporting Information). Likewise, the AC-field-dependent evolution of the dielectric constant (Figure 4b) for all $Pb_{1-x}Sr_xHfO_3$ compositions was examined. A typical ferroelectric material is expected to display a peak in the dielectric response upon increasing the AC electric field due to the increase in the ferroelectric domain-wall contribution to the dielectric constant.^[51] Antiferroelectric materials are expected to exhibit a similar behavior, but at a relatively higher applied AC electric field (i.e., at values corresponding to the antiferroelectric-to-ferroelectric phase transition, E_F).^[52,53] Below E_F , however, antiferroelectric $PbZrO_3$ thin films have been found to exhibit a weak residual ferroelectric phase^[54] due to unbalanced antiparallel shift of oxygen atoms along the [001]. A similar AC field-dependent dielectric response with a peak at ≈ 23 kV cm⁻¹ was observed for $PbHfO_3$ which can be considered as an additional attribute associated with its antiferroelectric nature. The peak in dielectric response, however, was found to diminish in $Pb_{1-x}Sr_xHfO_3$ solid solutions with increasing strontium content, until the system ultimately exhibits a fixed dielectric constant value with increasing applied AC electric field. This indicates diminishing antiferroelectric behavior in $Pb_{1-x}Sr_xHfO_3$ ($x > 0$) compositions as compared to $PbHfO_3$. Further, the absence of peaks in the switching current hysteresis loops (as compared to $PbHfO_3$) also reinforces the idea of a reduction in or absence of the antiferroelectric state in $Pb_{1-x}Sr_xHfO_3$ ($x > 0$).^[53]

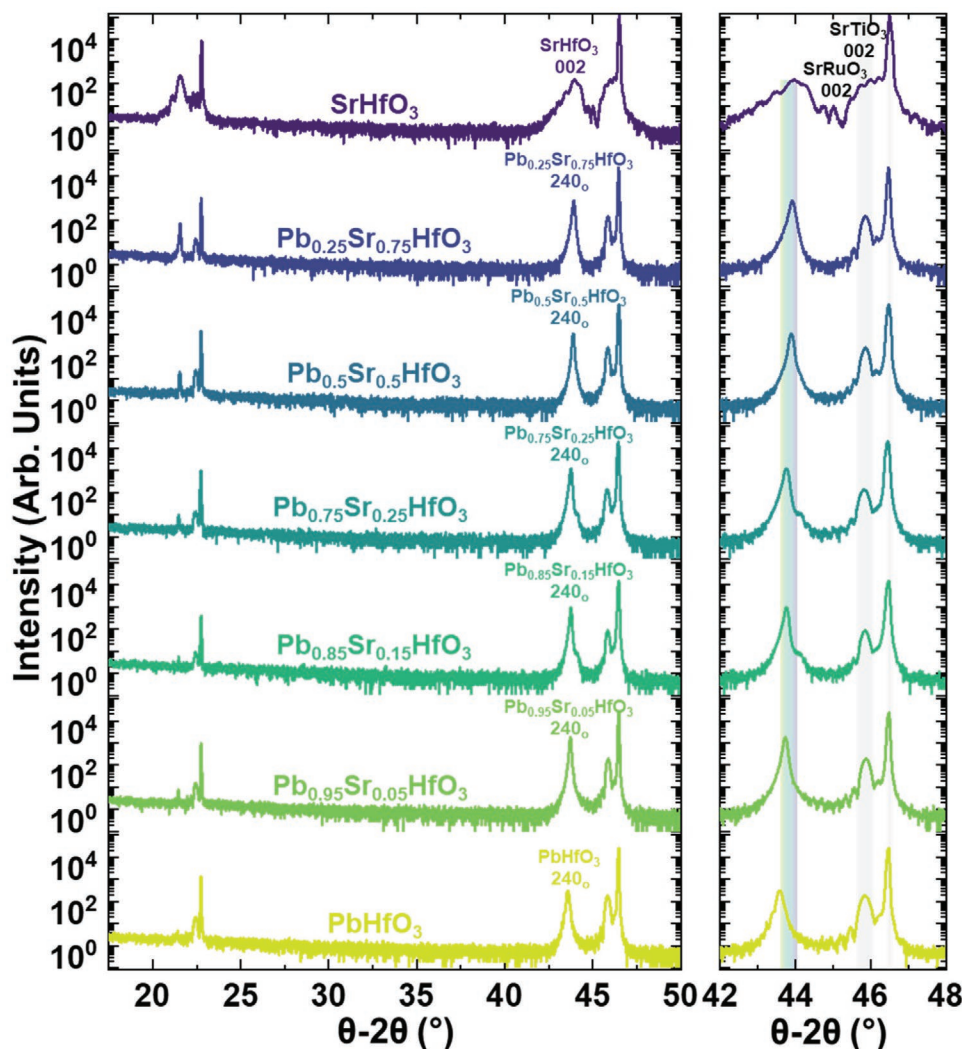


Figure 3. X-ray diffraction measurement (wide-angle θ - 2θ line scan, left) for 75-nm-thick epitaxial (240_{o})-oriented $\text{Pb}_{1-x}\text{Sr}_x\text{HfO}_3$ ($x = 0, 0.05, 0.15, 0.25, 0.5, 0.75, 1$) thin films on SrTiO_3 (001) substrates grown at a heater temperature ($600\text{ }^{\circ}\text{C}$), laser fluence (1.7 J cm^{-2}), and at dynamic oxygen partial pressure 10 mTorr. A zoom-in about the 240_{o} -diffraction condition for $\text{Pb}_{1-x}\text{Sr}_x\text{HfO}_3$ (right) includes a peak corresponding to the 002_{pc} -diffraction condition for SrRuO_3 .

We also probed the effect of strontium substitution on the E_{B} by measuring the polarization response as a function of electric field for 15 capacitors for the various $\text{Pb}_{1-x}\text{Sr}_x\text{HfO}_3$ films up to their electrical breakdown and used the Weibull-distribution function (Experimental Section) to extract a statistically meaningful breakdown field for each material (Figure 4c and Figure S14, Supporting Information).^[55] The highest $E_{\text{B}} = 5.12 \pm 0.5\text{ MV cm}^{-1}$ was observed for $\text{Pb}_{0.5}\text{Sr}_{0.5}\text{HfO}_3$ which is three times the value obtained for PbHfO_3 (1.23 MV cm^{-1}). Multiple parameters can affect the E_{B} of a dielectric capacitor, including the dielectric constant, leakage-current density (Figure S15, Supporting Information), electronic bandgap, microstructure, sample thickness, defect chemistry, electrode configuration, etc.^[56] Considering that the growth parameters, sample geometry and thickness, and electrode configuration for the various $\text{Pb}_{1-x}\text{Sr}_x\text{HfO}_3$ heterostructures are identical, the variables most likely to alter the E_{B} of the different $\text{Pb}_{1-x}\text{Sr}_x\text{HfO}_3$ ($0 < x < 1$) compositions are likely the bandgap and dielectric constant. The

experimentally reported optical band-gap values for PbHfO_3 and SrHfO_3 are $3.4^{[18]}$ and 6.1 eV ,^[24] respectively. Thus, strontium substitution could potentially improve the E_{B} performance by either (or both) increasing the bandgap and/or decreasing the dielectric constant. Additionally, there can be changes to the leakage current density (i.e., the higher the leakage current density, the lower the E_{B}) with strontium substitution which can contribute to altering the E_{B} . While we can confirm the effect of strontium on the dielectric permittivity and leakage current density, additional optical studies are required to explore the bandgap aspect. Next, the polarization response was measured for all the compositions driven up to their corresponding E_{B} values [i.e., PbHfO_3 ($\pm 1.23\text{ MV cm}^{-1}$), $\text{Pb}_{0.95}\text{Sr}_{0.05}\text{HfO}_3$ ($\pm 3.52\text{ MV cm}^{-1}$), $\text{Pb}_{0.85}\text{Sr}_{0.15}\text{HfO}_3$ ($\pm 3.52\text{ MV cm}^{-1}$), $\text{Pb}_{0.75}\text{Sr}_{0.25}\text{HfO}_3$ ($\pm 3.94\text{ MV cm}^{-1}$), $\text{Pb}_{0.5}\text{Sr}_{0.5}\text{HfO}_3$ ($\pm 5.12\text{ MV cm}^{-1}$), and $\text{Pb}_{0.25}\text{Sr}_{0.75}\text{HfO}_3$ ($\pm 2.31\text{ MV cm}^{-1}$)] at 10 kHz (Figure 4d). The saturation polarization for all the compositions was found to vary from 0.3 to $44\text{ }\mu\text{C cm}^{-2}$ depending on the extent of

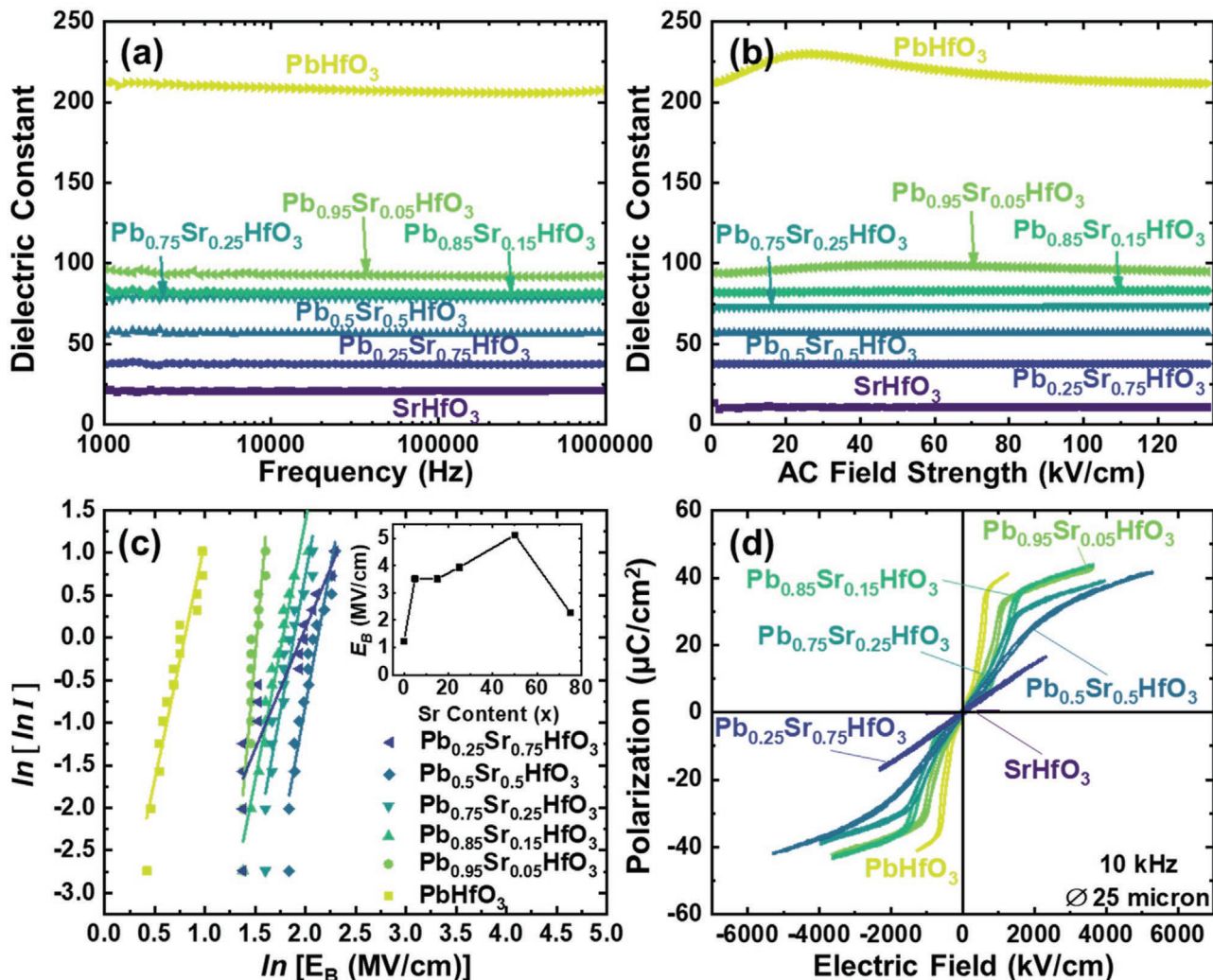


Figure 4. Dielectric and polarization response of 75-nm-thick epitaxial (240_O)-oriented Pb_{1-x}Sr_xHfO₃ ($x=0, 0.05, 0.15, 0.25, 0.5, 0.75, 1$) thin films on SrTiO₃ (001) substrates. Dielectric constant measurements as a function of a) frequency from 1 to 1000 kHz and b) applied AC electric field up to 133 kV cm⁻¹ at a frequency of 10 kHz. c) Weibull analysis for determination of electric-breakdown strength (E_B) where I on the y-axis represents $\frac{1}{1-i}$; inset shows the variation in E_B as a function of strontium content in Pb_{1-x}Sr_xHfO₃ solid solution compositions. d) Polarization versus electric field hysteresis loop measurements as a function of 10 kHz with capacitors 25 μ m in diameter driven up to their respective E_B values.

strontium substitution (x) (i.e., a smaller value of polarization was observed at a given applied electric field with increasing strontium content).

Using these data, we can also explore the evolution of capacitive energy storage performance. The values for U_r and the overall efficiency η were extracted for all compositions (Figure 5a). Apart from an increase in E_B contributing to an increase in U_r , the decrease in U_{loss} (area enclosed within the polarization-electric field hysteresis loop) also played a significant role in the enhancement of the overall efficiency of the solid solutions. As seen in the trend for E_B , Pb_{0.5}Sr_{0.5}HfO₃ was found to exhibit the best energy-storage performance with a $U_r = 77 \pm 5$ J cm⁻³ and $\eta = 97 \pm 2\%$. This corresponds to a 2.7 times increase in U_r from 21 J cm⁻³ in PbHfO₃ with a remarkable η . Another important aspect for capacitive-energy storage is the need for significant electric fatigue resistance and thermal endurance, with both being essential for maintaining

the physical and operational integrity of the devices over a long period of use. The fatigue of two compositions ($x = 0$ and 0.5) was measured by repeatedly cycling the devices and measuring the polarization-electric field hysteresis loops as a function of the number of cycles at $E_{max} = 1.23, 3,$ and 5.12 MV cm⁻¹ (Experimental Section). The PbHfO₃ heterostructures were found to break down after ≈ 900 cycles (Figure S16a, Supporting Information) at $E_B = 1.23$ MV cm⁻¹, whereas the Pb_{0.5}Sr_{0.5}HfO₃ heterostructures did not show any cyclic fatigue even after 10⁹ cycles (a 10⁶ times improvement in fatigue endurance). Furthermore, while the PbHfO₃ heterostructures could not sustain any fatigue measurements at $E_{max} = 3$ and 5.12 MV cm⁻¹, the Pb_{0.5}Sr_{0.5}HfO₃ heterostructures sustained 3×10^5 and 7×10^4 cycles, respectively (Figure S17a-c, Supporting Information). The U_r and η values for PbHfO₃ and Pb_{0.5}Sr_{0.5}HfO₃ as a function of number of cycles are summarized (Figure 5b) wherein the Pb_{0.5}Sr_{0.5}HfO₃ heterostructures exhibit no significant

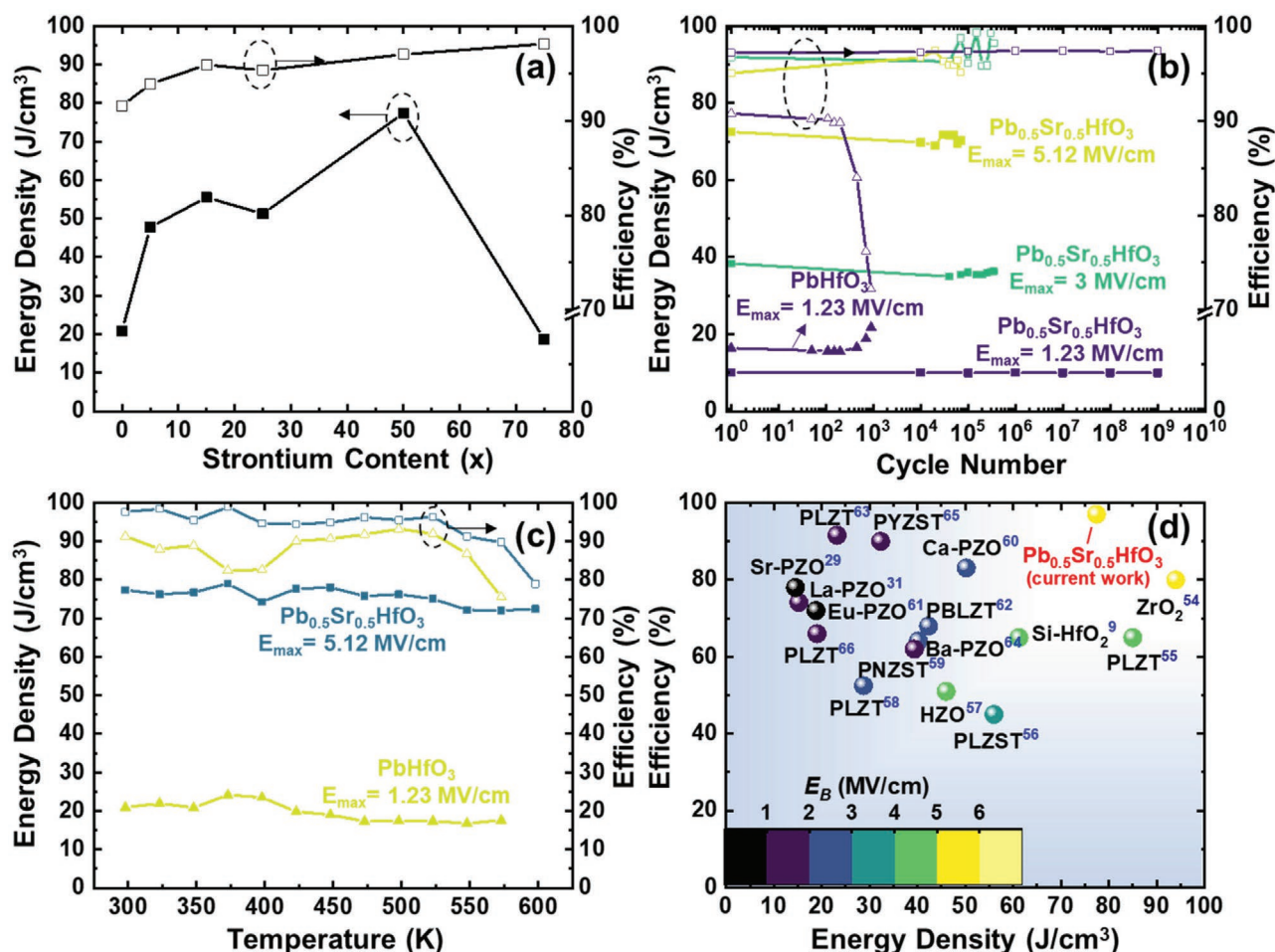


Figure 5. Energy-storage performance for 75-nm-thick epitaxial (240_o)-oriented $\text{Pb}_{1-x}\text{Sr}_x\text{HfO}_3$ ($x = 0, 0.05, 0.15, 0.25, 0.5, 0.75, 1$) thin films on SrTiO_3 (001) substrates. a) Plot of energy density (left-axis) and efficiency (right-axis) as a function of strontium content (x). b) Cyclic fatigue at a frequency of 10 kHz at electric field values of 1.23, 3, and 5.12 MV cm^{-1} for $\text{Pb}_{0.5}\text{Sr}_{0.5}\text{HfO}_3$ and 1.23 MV cm^{-1} for PbHfO_3 . c) Temperature (298–573 K) evolution of the energy storage density at the corresponding E_B values for PbHfO_3 and $\text{Pb}_{0.5}\text{Sr}_{0.5}\text{HfO}_3$ compositions. d) Summary of energy density and efficiency values for antiferroelectric materials reported in the recent past.

degradation in terms of their capacitive energy storage performance. Additionally, the thermal endurance of the PbHfO_3 and $\text{Pb}_{0.5}\text{Sr}_{0.5}\text{HfO}_3$ heterostructures was tested by performing polarization-electric field hysteresis loop measurements up to their respective E_B values as a function of temperature (298–573 K) (Figures S16b and S17d, Supporting Information). Though the U_r and η values degraded at higher temperatures in both compositions, the percentage change in U_r was lower in $\text{Pb}_{0.5}\text{Sr}_{0.5}\text{HfO}_3$ (6.5%) as compared to that in PbHfO_3 (15.9%) making it a better candidate for capacitive energy storage (Figure 5c). This claim is further supported by the fact that the U_r and η values for the $\text{Pb}_{0.5}\text{Sr}_{0.5}\text{HfO}_3$ films are on par with (or better than) those of all antiferroelectric materials reported in the literature (Figure 5d^[9,29,31,57–69]). All studies on (chemically modified) antiferroelectric thin films for capacitive energy storage applications have focused on three material systems: PbZrO_3 , $(\text{Pb}_{1-x}\text{La}_x)(\text{Zr}_{1-y-z}\text{Ti}_y\text{Nb}_z)\text{O}_3$, and HfO_2 .^[55] To the best of our knowledge, there have been no studies on the energy-storage behavior of $\text{Pb}_{1-x}\text{Sr}_x\text{HfO}_3$ single-crystalline films. A literature review (Figure 5d) shows that obtaining high U_r and η

values concomitantly in antiferroelectric materials is immensely challenging. In the current work, however, we have successfully obtained a significantly high U_r ($77 \pm 5 \text{ J cm}^{-3}$) along with an unusually high η ($97 \pm 2\%$) by virtue of the reduction of hysteresis loss and enhancement of E_B by chemically modifying the antiferroelectric PbHfO_3 , thus providing tremendous potential for implementation in real-life device applications.

3. Conclusion

Here, we showed that it is possible to synthesize high-quality epitaxial thin films of orthorhombic (240_o)-oriented PbHfO_3 and cubic (001)-oriented SrHfO_3 on SrTiO_3 (001) (and other) substrates. This was followed by structural, dielectric, and electrical characterization of the as-grown heterostructures. While PbHfO_3 films demonstrated robust antiferroelectric properties, SrHfO_3 heterostructures did not exhibit ferroelectric behavior across the temperature range (77–623 K) studied nor under applied electric fields (-3 to 3 MV cm^{-1}). The lack of a long-

range polar order in SrHfO₃ was contextualized by first-principles studies that found that there is only a small energy change within the accuracy of our calculations ($\Delta E = 0.62$ meV/atom) associated with the structural distortion from the nonpolar ($Pm\bar{3}m$) to the polar ($P4mm$) phase. Additionally, we evaluated the synthesis and capacitive energy storage performance of Pb_{1-x}Sr_xHfO₃ ($x = 0, 0.05, 0.15, 0.25, 0.5, 0.75, 1$) thin-film heterostructures on SrTiO₃ (001) substrates. It was observed that increasing the strontium content leads to an increase in E_B as well as a decrease in U_{loss} resulting in considerable enhancement of U_r and η at optimum compositions (Pb_{0.5}Sr_{0.5}HfO₃). This optimized material provided strong all-around performance as a potential candidate for capacitive-energy-storage applications, with $E_B = 5.12 \pm 0.5$ MV cm⁻¹, $U_r = 77 \pm 5$ J cm⁻³, and $\eta = 97 \pm 2\%$, accompanied by fatigue endurance and thermal stability comparable to that of the best known antiferroelectric and/or paraelectric oxides reported in the literature.

4. Experimental Section

Growth of Thin-Film Heterostructures: All thin-film heterostructures were grown using pulsed-laser deposition in an on-axis geometry with a target-to-substrate distance of 55 mm, using a KrF excimer laser (248 nm, LPX 300, Coherent). All thin-film heterostructures with compositions of PbHfO₃ and SrHfO₃ were grown from ceramic targets with 45–50-nm-thick SrRuO₃ layers as the top and bottom electrodes. Multiple targets were tested for the growth of the PbHfO₃ thin films (i.e., PbHfO₃, Pb_{1.1}HfO₃, Pb_{1.2}HfO₃) to account for the potentially volatile nature of lead. In the end, stoichiometric PbHfO₃ films can be obtained from the different target compositions by carefully controlling various growth parameters. For PbHfO₃, 15–360-nm-thick films were deposited on multiple substrates [i.e., SrTiO₃ (001), TbScO₃ (110), and MgO (001)], at heater temperatures from 600 to 650 °C, across a range of dynamic oxygen-partial pressures (10–100 mTorr), laser fluence values (1.4–2 J cm⁻²), and at a laser repetition rate of 10 Hz. The oxygen-partial pressure was maintained at a constant value in this range by striking a balance between the flow rate of oxygen into the chamber and the rate at which the oxygen was being pumped out of the chamber. The SrHfO₃ thin films were grown from targets with the same nominal composition. For SrHfO₃, 30–400-nm-thick films were deposited on multiple substrates [i.e., SrTiO₃ (001), SrTiO₃ (110), and NdScO₃ (110)] at a range of heater temperatures (600–850 °C), across various dynamic oxygen-partial pressures (1–100 mTorr), laser fluence values (0.75–2.5 J cm⁻²), and laser repetition rates (1–20 Hz). The composition of the Pb_{1-x}Sr_xHfO₃ thin-film heterostructures was varied across $0 < x < 1$ through sub-unit-cell-level mixing using two ceramic targets with composition PbHfO₃ and SrHfO₃ via a programmable target rotator (Neocera, LLC) that was synced with the excimer laser. The growth of the 75-nm-thick Pb_{1-x}Sr_xHfO₃ ($0 < x < 1$) films was done on SrTiO₃ (001) substrates at a heater temperature of 600 °C, a dynamic oxygen pressure of 10 mTorr, a laser fluence of 1.93 J cm⁻², and a laser repetition rate of 10 Hz. In all growths for PbHfO₃, SrHfO₃, and Pb_{1-x}Sr_xHfO₃ ($0 < x < 1$), the heterostructures were cooled from the growth temperature to room temperature at 10 °C min⁻¹ in a static oxygen pressure of ≈760 Torr.

Chemical Analysis: To determine the stoichiometry of the PbHfO₃ films grown across a range of dynamic oxygen-partial pressures (10–100 mTorr), Rutherford backscattering spectrometry (RBS) was performed on the PbHfO₃ films grown on Al₂O₃ (0001) (sapphire) substrates using a National Electrostatics Corp. Model 5SDH pelletron tandem accelerator. This involved a beam of monoenergetic (3.040 MV) and collimated alpha particles (⁴He nuclei) being made incident on the film surface at an incident angle $\alpha = 22.5^\circ$, exit angle $\beta = 25.35^\circ$, and with a scattering angle $\theta = 168^\circ$. The spectrum was fitted using the software SIMNRA to obtain the molar ratio of the lead and hafnium for PbHfO₃.

Determination of Crystal Structure via X-Ray Diffraction: The crystal structure of the synthesized epitaxial films was determined using X-ray diffraction studies performed using a high-resolution X-ray diffractometer (Panalytical, X'Pert³ MRD) with fixed-slit, 1/2° and 1/16° incident optics, copper K α radiation (1.54 Å), and a receiving slit of 0.275 mm for the PIXcel3D-Medipix3 detector. θ -2 θ line scans were performed to probe the structure in the direction perpendicular to the plane of the substrate and X-ray rocking curves were completed about the Pb_{1-x}Sr_xHfO₃ ($0 \leq x < 1$) 240₀- and SrHfO₃ 002-diffraction conditions for the different substrates to assess the crystalline quality of the heterostructures. Asymmetric azimuthal scans were carried out about the PbHfO₃ 362₀-, SrHfO₃ 103-, SrHfO₃ 101-, and SrTiO₃ 103-diffraction conditions varying the angle at a fixed 2 θ value. Additionally, to determine the crystal structure and the lattice parameters of the heterostructures with composition Pb_{1-x}Sr_xHfO₃ ($0 \leq x \leq 1$), X-ray diffraction RSM studies were performed about the 362₀-, 084₀-, 240₀-diffraction conditions of the films and 103-diffraction condition of the substrate.

Electrical and Dielectric Characterization: The electrical properties for all the heterostructures of all compositions [Pb_{1-x}Sr_xHfO₃ ($0 \leq x \leq 1$)] were studied for films grown on SrTiO₃ (001) substrates wherein 45–50-nm-thick SrRuO₃ films served as both top and bottom electrodes. The measurements were performed with circular-capacitor (diameter 25 and 50 μ m) structures patterned on the top electrode using wet chemical etching via 0.1 M NaO₄ solution. The polarization as a function of electric field (–10 to 10 MV cm⁻¹) for these circular capacitor structures was measured using a Precision Multiferroic Tester (Radiant Technologies, Inc.) as a function of temperature (77–673 K). Dielectric and loss tangent measurements were performed using an E4990A Impedance Analyzer (Keysight Technologies) as a function of temperature (77–673 K) and frequency (1–1000 kHz) up to an AC field strength value of 275 kV cm⁻¹. The fatigue behavior was probed via pulsed measurements using a triangular waveform as the excitation pulse applied at a frequency 10 kHz up to 10⁹ cycles.

First-Principles Calculations: Density functional theory calculations were performed using the projector augmented wave (PAW) formalism as implemented within VASP.^[70] Within DFT, total energies and structural parameters can be very sensitive to convergence thresholds and the choice of exchange-correlation functional. While PBE gradient-corrected functionals are considered reliable for a wide range of material systems, these functionals can be subject to “super-tetragonality” errors in certain ferroelectrics and can overestimate both lattice distortions and spontaneous polarizations.^[48,71] Therefore, the referenced high-throughput workflow^[46] was run separately with the LDA and PBE functionals. In both cases, the 5p, 6s, and 5d electrons of the hafnium cations were treated explicitly as valence, as were the 4s, 4p, and 5s electrons in strontium cations and the 2s and 2p electrons in oxygen anion. A plane-wave energy cutoff of 740 eV was used, and Brillouin-zone integrations were performed with the tetrahedron method with Blöchl corrections,^[72] using a 9 × 9 × 9 Gamma-centered k-point grid. The calculations were scalar relativistic, but spin-orbit coupling was neglected. The initial SrHfO₃ crystal structure atomic coordinates for the $Pm\bar{3}m$ and $P4mm$ phases were obtained from the *Materials Project* database and then fully relaxed until all forces were smaller than 10⁻⁵ eV Å⁻¹ (Supporting Information). To calculate the polarization, the procedure implemented in *pymatgen*'s analysis ferroelectricity module was followed, which is described in detail in the referenced high-throughput workflow.^[46] Interpolation paths containing ten structures were chosen, and the spontaneous polarization was computed using the Berry-phase approach, following the module's documentation.

Supporting Information

Supporting Information is available from the Wiley Online Library or from the author.

Acknowledgements

This work was primarily supported by the U.S. Department of Energy, Office of Science, Office of Basic Energy Sciences, Materials Sciences and Engineering Division under Contract No. DE-AC02-05-CH11231 (Materials Project program KC23MP) for the discovery of novel functional materials. Computational resources used at the Molecular Foundry were supported by the U.S. Department of Energy, Office of Science, Office of Basic Energy Sciences under Contract No. DE-AC02-05CH11231. Additional computational resources were provided by NERSC. E.B. acknowledges support from the National Science Foundation Graduate Research Fellowship under Grant No. 1752814. M.R. acknowledges support from the National Science Foundation under Grant No. DMR-1708615. Y.J. acknowledges support from the Army Research Office under Grant No. W911NF-21-1-0126. A.F. acknowledges support from the Army Research Office under Grant No. W911NF-21-1-0118. A.D. acknowledges support from the Army Research Office under the ETHOS MURI via cooperative agreement W911NF-21-2-0162. B.H. acknowledges support from the Army Research Laboratory/Army Research Office via the Collaborative for Hierarchical Agile and Resonant Materials (CHARM) under cooperative agreement W911NF-19-2-0119.

Conflict of Interest

The authors declare no conflict of interest.

Data Availability Statement

Research data are not shared.

Keywords

antiferroelectrics, dielectrics, energy storage, hafnate, pulsed-laser deposition

Received: August 1, 2021
Revised: September 14, 2021
Published online: October 15, 2021

- [1] K. Black, M. Werner, R. Rowlands-Jones, P. R. Chalker, M. J. Rosseinsky, *Chem. Mater.* **2011**, *23*, 2518.
- [2] S. Migita, Y. Morita, M. Masahara, H. Ota, *Jpn. J. Appl. Phys.* **2014**, *53*, 04EA03.
- [3] J. Müller, T. S. Böske, S. Müller, E. Yurchuk, P. Polakowski, J. Paul, D. Martin, T. Schenk, K. Khullar, A. Kersch, W. Weinreich, S. Riedel, K. Seidel, A. Kumar, T. M. Arruda, S. V. Kalinin, T. Schlösser, R. Boschke, R. van Bentum, U. Schröder, T. Mikolajick, *2013 IEEE Int. Electron Devices Meet.* **2013**, 10.8.1.
- [4] M. H. Park, Y. H. Lee, T. Mikolajick, U. Schroeder, C. S. Hwang, *MRS Commun.* **2018**, *8*, 795.
- [5] Z. Lu, W. Bao, G. Wang, S. Sun, L. Li, J. Li, H. Yang, H. Ji, A. Feteira, D. Li, F. Xu, A. K. Kleppe, D. Wang, S. Liu, I. M. Reaney, *Nano Energy* **2021**, *79*, 105423.
- [6] T. Zhang, Y. Zhao, W. Li, W. Fei, *Energy Storage Mater.* **2019**, *18*, 238.
- [7] M. D. Nguyen, E. P. Houwman, M. T. Do, G. Rijnders, *Energy Storage Mater.* **2020**, *25*, 193.
- [8] W. Chao, T. Yang, Y. Li, *J. Mater. Chem. C* **2020**, *8*, 17016.
- [9] F. Ali, X. Liu, D. Zhou, X. Yang, J. Xu, T. Schenk, J. Muller, U. Schroeder, F. Cao, X. Dong, *J. Appl. Phys.* **2017**, *122*, 144105.
- [10] M. G. Kozodaev, A. G. Chernikova, R. R. Khakimov, M. H. Park, A. M. Markeev, C. S. Hwang, *Appl. Phys. Lett.* **2018**, *113*, 123902.
- [11] M. H. Park, H. J. Kim, Y. J. Kim, T. Moon, K. D. Kim, C. S. Hwang, *Nano Energy* **2015**, *12*, 131.
- [12] G. Shirane, *Phys. Rev.* **1952**, *86*, 219.
- [13] M. F. Kuprianov, S. M. Zaitsev, E. S. Gagarina, E. G. Fesenko, *Phase Transitions* **1983**, *4*, 55.
- [14] D. L. Corker, A. M. Glazer, W. Kaminsky, R. W. Whatmore, J. Dec, K. Roleder, *Acta Crystallogr., Sect. B: Struct. Sci.* **1998**, *54*, 18.
- [15] S. Huband, A. M. Glazer, K. Roleder, A. Majchrowski, P. A. Thomas, *J. Appl. Crystallogr.* **2017**, *50*, 378.
- [16] K. Roleder, M. Maglione, M. D. Fontana, I. Jankowska-Sumara, G. E. Kugel, J. Dec, *Ferroelectrics* **2000**, *238*, 139.
- [17] F. Jona, G. Shirane, F. Mazzi, R. Pepinsky, *Phys. Rev.* **1957**, *105*, 849.
- [18] O. I. Prokopalov, I. P. Raevskii, M. A. Malitskaya, Y. M. Popov, A. A. Bokov, V. G. Smotrakov, *Ferroelectrics* **1982**, *45*, 89.
- [19] X. Huang, T. Zhang, W. Wang, P. Ge, X. Tang, *Mater. Des.* **2021**, *204*, 109666.
- [20] B. Hanrahan, C. Milesi-Brault, A. Leff, A. Payne, S. Liu, M. Guennou, N. Strnad, *APL Mater.* **2021**, *9*, 021108.
- [21] X. Huang, T. Zhang, R. Gao, H. Huang, P. Ge, H. Tang, X. Tang, *ACS Appl. Mater. Interfaces* **2021**, *13*, 21331.
- [22] B. J. Kennedy, C. J. Howard, B. C. Chakoumakos, *Phys. Rev. B: Condens. Matter Mater. Phys.* **1999**, *60*, 2972.
- [23] M. K. Singh, G. Singh, T. H. Kim, S. Kojima, R. S. Katiyar, J. F. Scott, *EPL* **2014**, *107*, 26004.
- [24] M. Sousa, C. Rossel, C. Marchiori, H. Siegwart, D. Caimi, J. P. Locquet, D. J. Webb, R. Germann, J. Fompeyrine, *J. Appl. Phys.* **2007**, *102*, 104103.
- [25] M. Karmaoui, E. V. Raman, D. M. Tobaldi, L. Lajaunie, M. P. Graça, R. Arenal, M. P. Seabra, J. A. Labrincha, R. C. Pullar, *RSC Adv.* **2016**, *6*, 51493.
- [26] H. Murata, T. Yamamoto, H. Moriwake, I. Tanaka, *Phys. Status Solidi B* **2009**, *246*, 1628.
- [27] L. M. Garten, S. Dwaraknath, J. Walker, J. S. Mangum, P. F. Ndione, Y. Park, D. A. Beaton, V. Gopalan, B. P. Gorman, L. T. Schelhas, M. F. Toney, S. Trolier-McKinstry, K. A. Persson, D. S. Ginley, *Adv. Mater.* **2018**, *30*, 1800559.
- [28] H. Ling, S. S. Dwaraknath, K. A. Persson, *Chem. Mater.* **2020**, *32*, 2836.
- [29] X. Hao, J. Zhai, X. Yao, *J. Am. Ceram. Soc.* **2009**, *92*, 1133.
- [30] J. D. Jackson, *Classical Electrodynamics*, Wiley, New York **1998**.
- [31] H. J. Lee, S. S. Won, K. H. Cho, C. K. Han, N. Mostovych, A. I. Kingon, S. Kim, H. Y. Lee, *Appl. Phys. Lett.* **2018**, *112*, 092901.
- [32] Y. Z. Li, J. L. Lin, Y. Bai, Y. Li, Z. D. Zhang, Z. J. Wang, *ACS Nano* **2020**, *14*, 6857.
- [33] J. Parui, S. B. Krupanidhi, *Appl. Phys. Lett.* **2008**, *92*, 192901.
- [34] K. Singh, *Ferroelectrics* **1989**, *94*, 433.
- [35] E. Breckenfeld, R. B. Wilson, L. W. Martin, *Appl. Phys. Lett.* **2013**, *103*, 082901.
- [36] S. K. Sharma, A. Jayaraman, C. P. Chowdhury, S. Y. Wang, *J. Raman Spectrosc.* **1994**, *25*, 331.
- [37] H. Fujishita, Y. Ishikawa, *Ferroelectrics* **2002**, *269*, 135.
- [38] O. E. Fesenko, L. E. Balyunis, *Ferroelectrics* **1980**, *29*, 95.
- [39] K. M. Rabe, *Antiferroelectricity in Oxides: A Reexamination. in Functional Metal Oxides*, (Eds: S. B. Ogale, T. V. Venkatesan, M. G. Blamire), Wiley-VCH, Weinheim, Germany **2013**.
- [40] D. Damjanovic, *Rep. Prog. Phys.* **1998**, *61*, 1267.
- [41] S. Saremi, R. Xu, L. R. Dedon, J. A. Mundy, S. Hsu, Z. Chen, A. R. Damodaran, S. P. Chapman, J. T. Evans, L. W. Martin, *Adv. Mater.* **2016**, *28*, 10750.
- [42] S. Saremi, R. Xu, L. R. Dedon, R. Gao, A. Ghosh, A. Dasgupta, L. W. Martin, *Adv. Mater. Interfaces* **2018**, *5*, 1700991.
- [43] P. H. Sun, T. Nakamura, Y. J. Shan, Y. Inaguma, M. Itoh, *Ferroelectrics* **1998**, *217*, 137.
- [44] M. Acharya, S. Mack, A. Fernandez, J. Kim, H. Wang, K. Eriguchi, D. Meyers, V. Gopalan, J. Neaton, L. W. Martin, *Chem. Mater.* **2020**, *32*, 7274.

- [45] M. G. Stachiotti, G. Fabricius, R. Alonso, C. O. Rodriguez, *Phys. Rev. B* **1998**, *58*, 8145.
- [46] R. Vali, *Solid State Commun.* **2008**, *148*, 29.
- [47] T. E. Smidt, S. A. Mack, S. E. Reyes-Lillo, A. Jain, J. B. Neaton, *Sci. Data* **2020**, *7*, 72.
- [48] Y. Zhang, J. Sun, J. P. Perdew, X. Wu, *Phys. Rev. B* **2017**, *96*, 035143.
- [49] M. Sawkar-Mathur, C. Marchiori, J. Fompeyrine, M. F. Toney, J. Bargar, J. P. Cang, *Thin Solid Films* **2010**, *518*, S118.
- [50] M. D. McDaniel, C. Hu, S. Lu, T. Q. Ngo, A. Posadas, A. Jiang, D. J. Smith, E. T. Yu, A. A. Demkov, J. G. Ekerdt, *J. Appl. Phys.* **2015**, *117*, 054101.
- [51] K. Wu, W. A. Schulze, *J. Am. Ceram. Soc.* **1992**, *75*, 3385.
- [52] K. Nadaud, C. Borderon, R. Renoud, M. Bah, S. Ginestar, H. W. Gundel, *Appl. Phys. Lett.* **2021**, *118*, 042902.
- [53] Z. Luo, X. Lou, F. Zhang, Y. Liu, D. Chang, C. Liu, Q. Liu, B. Dkhil, M. Zhang, X. Ren, H. He, *Appl. Phys. Lett.* **2014**, *104*, 142904.
- [54] M. D. Coulbaly, C. Borderon, R. Renoud, H. W. Gundel, *Appl. Phys. Lett.* **2020**, *117*, 142905.
- [55] W. J. Weibull, *Appl. Mech.* **1951**, *73*, 293.
- [56] H. Palneedi, M. Peddigari, G. Hwang, D. Jeong, J. Ryu, *Adv. Funct. Mater.* **2018**, *28*, 1803665.
- [57] S. Yi, H. Lin, M. Chen, *J. Mater. Chem. A* **2021**, *9*, 9081.
- [58] B. Ma, Z. Hu, R. E. Koritala, T. H. Lee, S. E. Dorris, U. Balachandran, *J. Mater. Sci.: Mater. Electron.* **2015**, *26*, 9279.
- [59] X. Hao, Y. Wang, L. Zhang, L. Zhang, S. An, *Appl. Phys. Lett.* **2013**, *102*, 163903.
- [60] M. H. Park, H. J. Kim, Y. J. Kim, T. Moon, K. D. Kim, C. S. Hwang, *Adv. Energy Mater.* **2014**, *4*, 1400610.
- [61] X. Hao, Y. Wang, J. Yang, S. An, J. Xu, *J. Appl. Phys.* **2012**, *112*, 114111.
- [62] B. Shen, Y. Li, N. Sun, Y. Zhao, X. Hao, *Nanoscale* **2020**, *12*, 8958.
- [63] Y. Z. Li, Z. J. Wang, Y. Bai, Z. D. Zhang, *J. Eur. Ceram. Soc.* **2020**, *40*, 1285.
- [64] M. Ye, Q. Sun, X. Chen, Z. Jiang, F. Wang, *J. Am. Ceram. Soc.* **2011**, *94*, 3234.
- [65] H. Gao, N. Sun, Y. Li, Q. Zhang, X. Hao, L. B. Kong, Q. Wang, *Ceram. Int.* **2016**, *42*, 16439.
- [66] M. D. Nguyen, C. T. Q. Nguyen, H. N. Vu, G. Rijnders, *J. Eur. Ceram. Soc.* **2018**, *38*, 95.
- [67] B. Peng, Q. Zhang, X. Li, T. Sun, H. Fan, S. Ke, M. Ye, Y. Wang, W. Lu, H. Niu, X. Zeng, H. Huang, *ACS Appl. Mater. Interfaces* **2015**, *7*, 13512.
- [68] C. W. Ahn, G. Amarsanaa, S. S. Won, S. A. Chae, D. S. Lee, I. W. Kim, *ACS Appl. Mater. Interfaces* **2015**, *7*, 26381.
- [69] J. Ge, X. Dong, Y. Chen, F. Cao, G. Wang, *Appl. Phys. Lett.* **2013**, *102*, 142905.
- [70] P. E. Blöchl, *Phys. Rev. B* **1994**, *50*, 17953.
- [71] D. I. Bilc, R. Orlando, R. Shaltaf, G.-M. Rignanese, J. Íñiguez, P. Ghosez, *Phys. Rev. B* **2008**, *77*, 165107.
- [72] P. E. Blöchl, O. Jepsen, O. K. Andersen, *Phys. Rev. B* **1994**, *49*, 16223.